Topologically Allowed Nonsixfold Vortices in a Sixfold Multiferroic Material: Observation and Classification

Shaobo Cheng,[1,2] Jun Li,[3] Myung-Geun Han,[2] Shiqing Deng,[1] Guotai Tan,[4] Xixiang Zhang,[3] Jing Zhu,[1,†] and Yimei Zhu[2,*]
[1]School of Materials Science and Engineering, Tsinghua University, Beijing 100084, People's Republic of China
[2]Department of Condensed Matter Physics and Materials Science, Brookhaven National Laboratory, Upton, New York 11973, USA
[3]Division of Physical Science and Engineering, King Abdullah University of Science and Technology, Thuwal 239955, Saudi Arabia
[4]Department of Physics, Beijing Normal University, Beijing 100875, People's Republic of China
(Received 10 June 2016; published 5 April 2017)

We report structural transformation of sixfold vortex domains into two-, four-, and eightfold vortices via a different type of topological defect in hexagonal manganites. Combining high-resolution electron microscopy and Landau-theory-based numerical simulations, we investigate the remarkable atomic arrangement and the intertwined relationship between the vortex structures and the topological defects. The roles of their displacement field, formation temperature, and nucleation sites are revealed. All conceivable vortices in the system are topologically classified using homotopy group theory, and their origins are identified.

DOI: 10.1103/PhysRevLett.118.145501

Topological structures emerging near spontaneous symmetry-breaking transitions are ubiquitously observed in wide branches of science [1–6]. In condensed matter, topologically protected defects can be promising candidates for information storage technology. Skyrmions, multiferroic vortices, domain walls, dislocations, and disclinations are examples where emergent properties and behaviors have been reported [7–12]. Investigation of these stable configurations is of great interest due to their fascinating underlying physics responsible for striking geometric patterns found in the order-parameter (OP) field [13]. Understanding topological structures is crucial to the prediction of the behavior and functionalities emerging from these topological defects [14,15]. However, to date, the interactions among topological defects have rarely been studied, largely due to the difficulties in experimental observation and validation. Understanding the interactions between topological defects might provide a new route to achieve programmable manipulation and control to yield emergent functionality.

In multiferroic hexagonal manganites $RMnO_3$ (R = rare earth), the crystal structure adopts centrosymmetric $P6_3/mmc$ (D_{6h}) at high temperature. A structural transition occurs at temperature T_s, which lowers the symmetry to $P6_3cm$ (C_{6v}) mainly by the condensation of the K_3 phonon mode. This process leads to the trimerized tilting of MnO_5 bipyramids and corrugation of intercalated R layers while maintaining the sixfold symmetry [Fig. 1(a)]. The condensation yields six possible azimuthal angles (φ) of the bipyramid tilting at an interval of $\pi/3$. Each value of φ is accompanied by a distinct corrugated configuration in R layers, in which two-thirds of R atoms shift up along the c axis and the rest shift down, as summarized in Fig. 1(b) [16–18]. Previous theoretical work suggests that the continuous symmetry of OP space at high temperature gives rise to the formation of vortex cores, while the discrete Z_6 symmetry at low temperature leads to the emergence of six bounded domain walls surrounding each vortex core [19–22]. With continuous symmetry of the degeneracy OP space, φ varies continuously around the cores. At low temperature, φ falls into one of the six preferred values with equal probability, and Z_6 symmetry becomes dominant in the system [19]. This process results in the emergence of six crystallographically preferred domains denoted as α^+, β^-, γ^+, α^-, β^+, γ^- or α^+, γ^-, β^+, α^-, γ^+, β^- (known as vortex and antivortex) in sequence around the core [16].

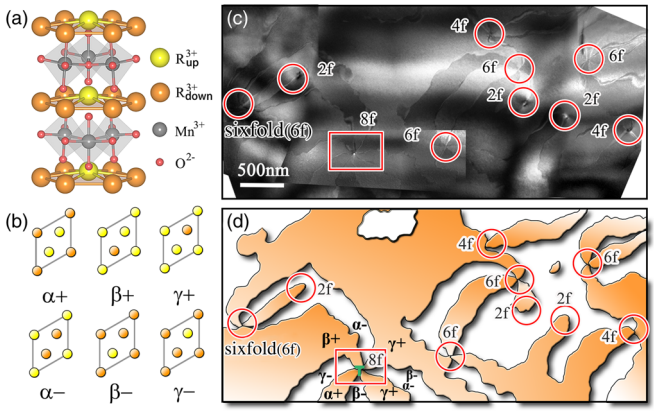

FIG. 1. Nonsixfold vortex domains in hexagonal $RMnO_3$. (a) Atomic unit cell showing the $P6_3cm$ symmetry with downward polarization. The yellow and orange spheres represent R ions at 2a and 4b Wyckoff positions, respectively. (b) Atomic models for three types of antiphase domains (α, β, γ) and two types of ferroelectric polarizations (+, −). (c) Composite of mesoscale dark-field TEM images with two-, four-, six-, and eightfold vortices marked by red circles and rectangle in $YMnO_3$. (d) The corresponding schematic diagram from (c).

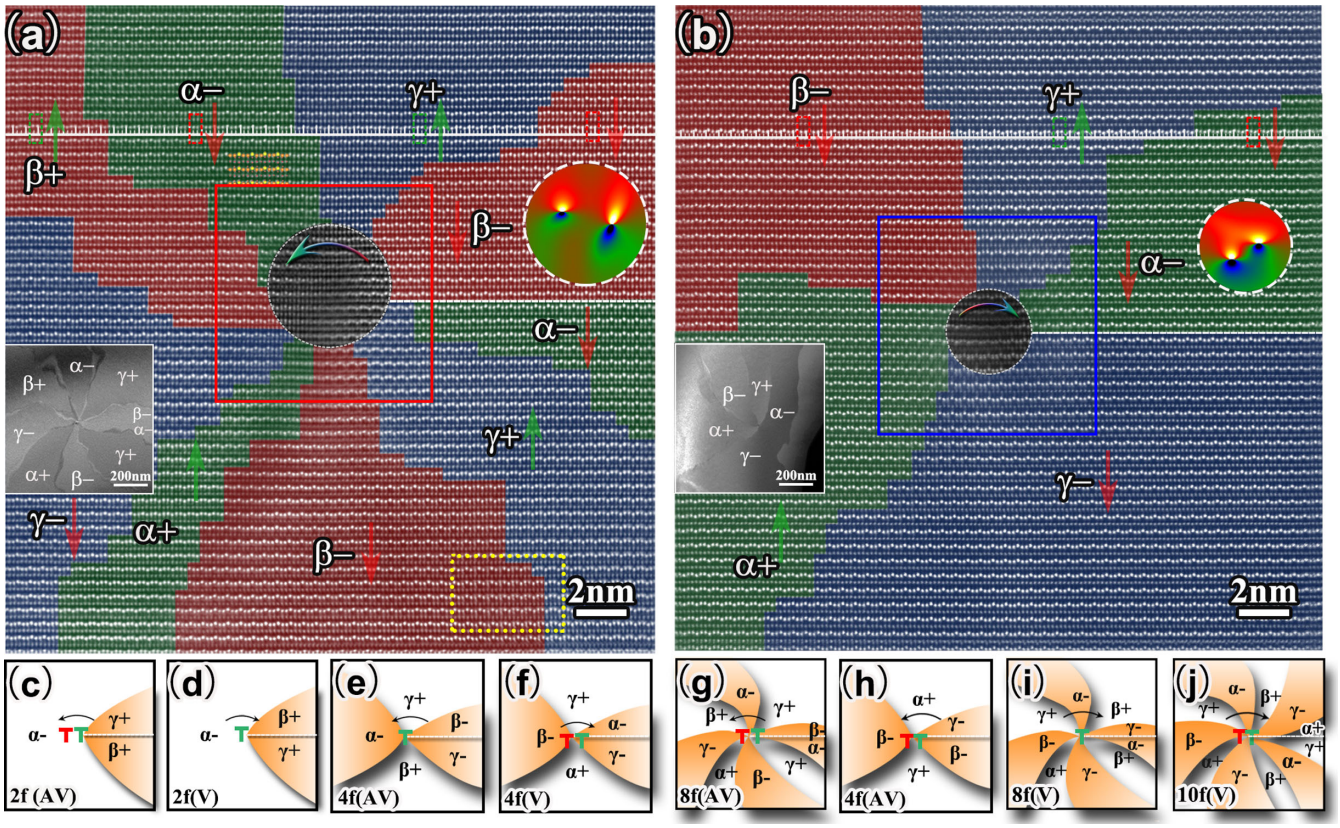

FIG. 2. Atomic images and schematic diagrams of nonsixfold vortices. (a),(b) High-resolution HAADF STEM images of eightfold antivortex (a) and fourfold vortex (b) structures viewed along the [100] axis in $YMnO_3$. The bright and less-bright atoms are Y and Mn ions, respectively. The white horizontal lines with tick marks in (a) and (b) are reference rulers to assist in identifying the translation relationship across the domain walls (small green and red dashed rectangles represent the unit cell with downward or upward polarization). Low magnification dark-field images and strain maps, where yellow, red, green, and blue represent the ε_{xx} values of $+8\%$, $+4\%$, -4%, and -8%, respectively, of the core areas are also included. The α, β, and γ are colored in green, red, and blue, respectively. The red, blue solid squares and yellow dotted rectangle are magnified [27]. (c)–(j) Schematics of eight possible nonsixfold vortices. The first five (c)–(g) are experimentally observed. AV, antivortex; V, vortex. Vortices shown in (a) and (b) can be topologically classified as $(-2)\times(-2)$ and $0\times(-2)$, and (c)–(j) can be classified as $(-1)\times(-2)$, $0\times(-1)$, $(-1)\times(-1)$, $0\times(-2)$, $(-2)\times(-2)$, $(-1)\times(-2)$, $1\times(-1)$, and $1\times(-2)$, respectively. The horizontal lines in (a)–(j) are the dividing lines for order parameter θ.

These sixfold vortices are topologically protected and extremely stable under thermal perturbation and external biasing [22–24]. The distributions and connections of (anti) vortex cores have been analyzed by graph theory [25,26]. However, with the help of dislocations, the domain sequences around the vortex cores can be changed. Here, we report the first experimental observations of nonsixfold vortex cores in $RMnO_3$ using advanced electron microscopy to reveal their formation origin at atomic scale. The coupling mechanisms are studied by numerical simulations based on Landau theory, and the vortices are topologically classified via homotopy group theory.

$YMnO_3$ single crystals were grown by the floating zone method. Electron microscopy work was carried out at Brookhaven National Lab using the JEOL ARM 200CF microscope equipped with two aberration correctors achieving a point resolution of 0.08 nm. For HAADF (high-angle annular-dark-field) imaging, a convergent angle of 21.2 mrad and a collection angle of 67–275 mrad were used. To reduce noise, Wiener filter was used for some HAADF images.

Figure 1(c) illustrates a mesoscale composite of dark-field images of hexagonal $YMnO_3$ showing the coexistence of various two-, four-, six-, and eightfold vortices (marked by red circles). The first-ever-observed eightfold (anti) vortex is highlighted with the red rectangle. Figure 1(d) is the schematic of domain configurations derived from Fig. 1(c). Careful examination indicates the existence of partial edge dislocations (PEDs) near the vortex cores. In the floating zone method, a dramatic change in the sample temperature during crystal growth might introduce PEDs.

Atomically resolved eightfold and fourfold vortex structures are shown in Figs. 2(a) and 2(b) [27]. In Fig. 2(a), domains with the same polarization direction and corrugation state are present in one vortex configuration (two α^-, β^-, and γ^+ domains in this case, energetically unstable in

traditional sixfold vortices) can be stabilized by PEDs. Similar labeling was applied to other types of nonsixfold vortices, including the fourfold vortex shown in Fig. 2(b). More analyses about the configurations of the domain boundaries are also provided [27]. To map the associated strain field of the PEDs of the eight- and fourfold vortex cores, we used geometric phase analyses (GPA) [35], and the strain field of ε_{xx} (the x axis is the [120] direction) around the PEDs in Figs. 2(a) and 2(b) were constructed from the atomic images. Clearly, the nonuniform displacement field near the vortex centers plays a significant role in altering the corrugated configuration of the vortex structure. The corresponding mesoscale dark-field images that possess dissimilar contrast for oppositely polarized ferroelectric domains due to the breaking of Friedel's law are also included [36]. Careful atomic image analysis suggests that the PED possesses a Burgers vector of 1/3 [120]. To avoid the energetically unfavorable configurations due to the presence of PEDs, the original sixfold winding sequence $\alpha^- \to \beta^+ \to \gamma^- \to \alpha^+ \to \beta^- \to \gamma^+$ is transformed into a fourfold winding $\alpha^- \to \beta^+ \to \gamma^- \to \beta^- \to \gamma^+$, and a fourfold domain is formed [Fig. 2(b)]. All our experimentally observed nonsixfold vortices are summarized in Figs. 2(c)–2(g), along with other three predicted configurations [Figs. 2(h)–2(j)].

In $R\mathrm{MnO_3}$, the formation process of sixfold vortices can be characterized by the variation of a two-component order-parameter field: tilting amplitude of $\mathrm{MnO_5}$ bipyramids Q and azimuthal angle φ [19,22,37,38]. The degeneracy OP space is composed of six distinct points at low temperature [Fig. 3(a)] and expands to the continuous circle at a temperature slightly below T_s. The radius of this circle is proportional to the value of Q, so the circle shrinks into a single point when $T \geq T_s$ ($Q = 0$) [22]. However, because of the additional structural displacement field induced by PEDs, these two components are not sufficient for depicting the domain patterns. We, thus, introduce another scalar order parameter θ for describing the $\mathbf{x}$ component of the displacement field [27]. This parameter reflects the geometric phase around dislocations and is directly related to the atomic displacements of R atoms [39–41]. The distribution of θ around an edge dislocation with $b = 1$ and $\upsilon = 0.3$ is shown in Fig. 3(b): θ increases continuously from 0 to 2π along any clockwise circular trajectory whose starting and ending point are on a dividing line [indicated in Fig. 3(b)], which is attached to the dislocation core. Considering this dislocation appears in a monodomain ($\varphi = 0$), the "up-down-down" corrugated configuration above the dividing line abruptly switches into "down-down-up" below the line. The mismatch of corrugated configurations across the dividing line indicates that this line acts like an antiphase domain wall which is not interlocked with ferroelectric boundaries. Since the dislocation is not perfect (for the perfect case, $b = 3n$; n is an arbitrary integer), it is always bounded by such a line [42,43]. Thus, the corrugated configurations can be modulated by θ, and the OP space for $R\mathrm{MnO_3}$ in which

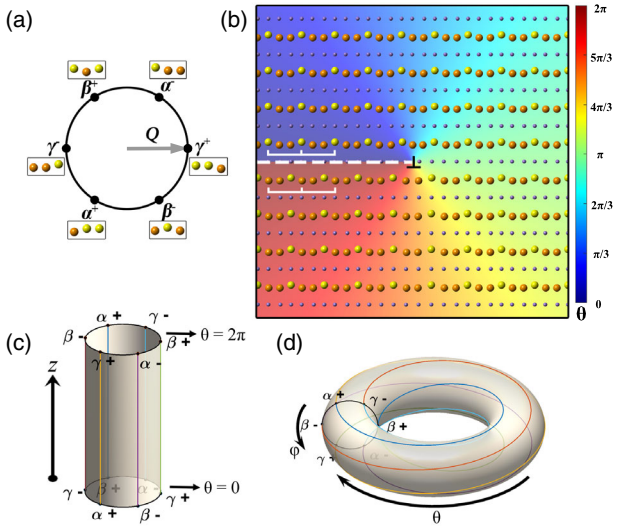

FIG. 3. (a) The OP space of a dislocation-free system. The six black points represent six degenerate states with Z_6 symmetry at low temperatures. The corresponding corrugated configurations of R atoms are also shown. Degeneracy space expands to the circle with continuous $U(1)$ symmetry as the temperature rises. The radius of this circle is proportional to Q. (b) A schematic shows the atomic structure around an edge dislocation with $b = 1$ in a monodomain. The field of OP θ is represented by the color legend. The dividing line (doted white line) indicates the position where θ discontinues. (c) The OP space of the $R\mathrm{MnO_3}$ system in which dislocations (vertical lines) exist. The value of θ varies from 0 to 2π along the z axis. (d) A toruslike OP space obtained by transforming the cylinder shown in (c): the two ends of this cylinder can be equivalent by twisting the cylinder (the α^+ point on the upper end aligns with the lower one along the z axis). With fixed θ, the variation of φ from 0 to 2π corresponds to a loop passing once through the smaller hole in the torus (the black circle). Similarly, as θ varies from 0 to 2π with $\varphi = 0$, its corresponding trajectory is the yellow line on the torus.

dislocations exist can be described by the surface of the cylinder [Fig. 3(c)]. By topological transformation of this cylinder, a toruslike OP space $\boldsymbol{V}$ can be obtained [Fig. 3(d)]. Hence, any closed loop in the system characterized by the (Q, φ, θ) field can be precisely mapped into a continuous trajectory in $\boldsymbol{V}$. More atomic models for two-, four-, and eightfold vortex core arrangements are provided [27]. Both experimental results and atomic models show that the corrugated configurations do not change significantly across dividing lines because the lattice jump induced by the dislocations is compensated by the changes of the corrugated configuration at the domain walls.

According to the homotopy group theory, for such a toruslike degeneracy space, all vortex configurations shown in Figs. 2(c)–2(g) can be classified by elements (m, n) of the fundamental homotopy group $\pi_1(\boldsymbol{R}) = Z \times Z$ [4,44,45]. This homotopy group is different from the one presented in Ref. [19], which is due to the expansion of OP space from a one-dimensional circle to a torus under the effect of PEDs. Considering a clockwise loop surrounding the vortex core

and its image trajectory in the OP space, the absolute value of integer m or n is the net number of times that the smaller or larger hole in the torus is circumnavigated by the trajectory, respectively. The values of m and n are positive when the circumnavigation directions are along the arrows indicated in Fig. 3(d) and negative when opposite the arrows. Based on this definition, n equals the Burgers vector b of the dislocation appearing in the core (for convenience, we treat the two adjacent PEDs with $b = 1$ as one PED with $b = 2$). All vortex configurations shown in Fig. 2 can be classified accordingly (see caption of Fig. 2). Generally, defects with lower winding numbers (i.e., smaller $|m|$ and $|n|$) are energetically preferred. It is also interesting to note that the number of ferroelectric domain walls bounded with a vortex core equals $|6m - 2n|$ [27]. Thus, a vortex core in our system should always be surrounded by an even number of domain walls.

To clarify the vortex-forming mechanism, we use the Landau phenomenological model for numerical simulations [27]. The newly defined angle parameter $(\varphi + \theta/3)$ ensures that the gradient energy density is continuous within domains, and dramatic variations take place only at ferroelectric domain walls and vortex cores. Based on this model, the annealing process can be simulated by the Monte Carlo method [22]. The vortex configurations of Figs. 2(c)–2(j) after annealing are shown in Figs. 4(a)–4(h). The temperature at which dislocations form T_d plays an important role in determining different classes of vortices in these simulations.

When dislocations form above the structural phase transition point T_s, classes of vortices labeled by $0 \times (\pm 1)$ and $0 \times (\pm 2)$ are those most frequently observed [Figs. 4(a) and 4(e)], and the $(\pm 1) \times (\pm 1)$, $(\pm 1) \times (\mp 1)$, $(\pm 1) \times (\pm 2)$, and $(\pm 1) \times (\mp 2)$ types can be occasionally observed [Figs. 4(b)–4(d) and 4(g)]. In this case, the initial distribution of φ is arbitrary and θ is given. As the temperature decreases from above T_s, the field of φ evolves adequately for lowering the local free energy. Thus, the vortices with lowest energy can be obtained during this process. This suggests that the twofold vortex with one dislocation in the core and fourfold vortex with two dislocations in the core are the most energetically preferred. As discussed in Ref. [22], the formation of sixfold vortex cores and domain walls in $R\mathrm{MnO}_3$ takes place right at the structural phase transition temperature. So, it is possible that the nucleation site of a vortex (i.e., the position around which φ varies from 0 to 2π continuously) is within or near a dislocation core region. In such a situation, vortices classified by $(\pm 1) \times n$ can be formed. Because of a higher gradient of the free energy density induced by a dramatically varying $(\varphi + \theta/3)$ field in the cores compared with the vortices with $m = 0$, the value of Q decreases noticeably in these regions.

By lowering T_d ($T_d < \frac{2}{3} T_s$), $[(\pm 1) \times n]$-type vortices become common, and the eightfold vortices classified by $(\pm 2) \times (\pm 2)$ can also be formed [Fig. 4(f)]. At $T = T_d$, the sixfold vortex pattern has already been formed, and the

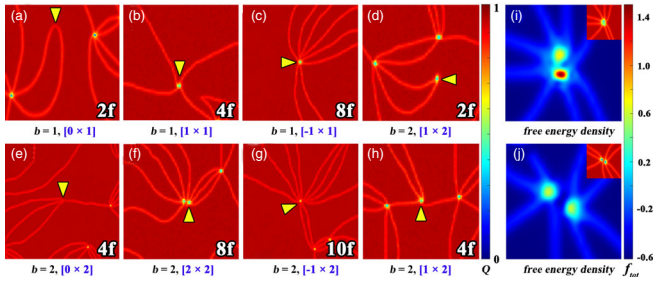

FIG. 4. Numerical simulations based on the Landau free energy model. (a)–(h) Coexistence of sixfold vortices and eight other types of dislocation-induced vortices showing the tilting amplitude Q of the OP field around the vortex cores. The yellow arrows indicate the position of the dislocations. Corresponding Burgers vectors b and fundamental homotopy group elements $[m \times n]$ are given at the bottom of each figure. Since the value of Q is slightly smaller at the domain walls than within the domains, the bright red lines indicate the position of the domain walls. Because of the high gradient free energy density in some types of vortex cores [(b)–(d) and (f)–(h)], Q decreases dramatically within these cores, which appear as yellow or green spots in these figures. By contrast, Q does not obviously decrease within the vortex cores where the density is relative low [(a),(e)]. Two spots are observed in (f) because the core is not stable and tends to split into two subcores. The color legend of Q is shown on the right with units of Å. (i) and (j) show the free-energy-density distributions around two (2×2)-type eightfold vortex cores obtained at two different dislocation formation temperatures T_d. The fission of the vortex core contributes to a reduction of the local free energy. Corresponding distributions of Q are given at the top right. The color legend of the free energy density is shown on the right with units of eV.

mobility of the vortex cores and domain walls is much lower than that at high temperatures. To balance the increased free energy induced by the displacement field, only relatively high-energy vortices form because the temperature is not sufficiently high to overcome the energy barrier blocking the formation of the $(0 \times n)$-type vortices. So, when one dislocation with $|b| = 2$ happens to locate within a sixfold vortex core at T_d, a $[(\pm 2) \times (\pm 2)]$-type vortex forms. In addition, a new type of fourfold vortex classified by $(\pm 1) \times (\pm 2)$ is also frequently observed when $T_d < \frac{2}{3} T_s$. Though it belongs to the same class as the twofold vortex shown in Fig. 4(d), the number of domain walls attached to the vortex core does not equal $|6m - 2n|$. This is because φ does not vary monotonically around the vortex core, and two separated areas have the same value of φ. However, these two areas can coalesce if they are near each other, and only two domain walls are left after the merge. Thus, these two kinds of $(\pm 1) \times (\pm 2)$ vortices are topologically identical.

It is noteworthy that the core of the $[(\pm 2) \times (\pm 2)]$-type vortex is not stable and tends to split into two adjacent vortices. For example, a (2×2)-type vortex core can split into a 1×2 (both fourfold and twofold vortices are

possible) vortex core and a 1×0 (sixfold) vortex core. Increased T_d usually leads to greater distance between these cores. By comparing Figs. 4(i) and 4(j), it is obvious that the free energy density of the unsplit eightfold vortex core obtained at $T_d = \frac{1}{6} T_s$ is higher than the energies of those two split cores obtained at $T_d = \frac{1}{2} T_s$. This result explains why the $[(\pm 2) \times (\pm 2)]$-type eightfold vortex is rarely seen in experiments.

In conclusion, using aberration-corrected electron microscopy, we revealed startling detailed atomic configurations of crystallographically forbidden nonsixfold ferroelectric domains surrounding the vortex cores in hexagonal $YMnO_3$. The unanticipated symmetry breaking was found at both mesoscale (domains) and atomic scale (vortex cores) due to the intertwining of two types of topological defects, i.e., (anti)vortex cores and PEDs. We showed that due to the interaction of PEDs with the surrounding lattice, the initially topologically protected sixfold (anti)vortex core structures can be transformed into other configurations. Thus, the PED, depending on its characteristics, including the Burgers vector, formation temperature, and nucleation sites, can behave as a control knob for regulating vortex domain symmetry. The ability to manipulate and control the ferroic orders in $RMnO_3$ in correlation with spontaneous magnetization, electric polarization, and spontaneous strain may provide a platform for exploring emerging physical phenomena with novel applications via topological defects.

The electronic microscopy work was carried out at Brookhaven National Laboratory and supported by the U.S. DOE Basic Energy Sciences, Materials Sciences and Engineering Division under Contract No. DE-SC0012704. J. Z., S. C., and S. D. would like to acknowledge the financial support by Chinese National Natural Science Foundation under Project No. 51390471 and the National 973 Project of China (Project No. 2015CB654902) as well as the support of S. C. for studying abroad from China Scholarship Council. The samples were prepared through the use of the resources of the National Center for Electron Microscopy in Beijing. The theoretic work was done at King Abdullah University of Science and Technology (KAUST) and supported by KAUST Office of Sponsored Research under Grant No. CRF-2015-2549-CRG4.

S. C. and J. L. contributed equally to this work.

*zhu@bnl.gov
†jzhu@mail.tsinghua.edu.cn

[1] T. W. B. Kibble, *Topological Defects and the Non-Equilibrium Dynamics of Symmetry Breaking Phase Transitions* (Springer, Dordrecht, 2000).
[2] I. A. Ovid'ko and A. E. Romanov, Commun. Math. Phys. **105**, 443 (1986).
[3] T. W. B. Kibble, J. Phys. A **9**, 1387 (1976).
[4] N. D. Mermin, Rev. Mod. Phys. **51**, 591 (1979).
[5] H. R. Trebin, Adv. Phys. **31**, 195 (1982).
[6] A. Vilenkin and E. P. S. Shellard, *Cosmic Strings and Other Topological Defects* (Cambridge University Press, Cambridge, England, 2000).
[7] X. Z. Yu, Y. Onose, N. Kanazawa, J. H. Park, J. H. Han, Y. Matsui, N. Nagaosa, and Y. Tokura, Nature (London) **465**, 901 (2010).
[8] H. Das, A. L. Wysocki, Y. Geng, W. Wu, and C. J. Fennie, Nat. Commun. **5**, 2998 (2014).
[9] D. Meier, J. Seidel, A. Cano, K. Delaney, Y. Kumagai, M. Mostovoy, N. A. Spaldin, R. Ramesh, and M. Fiebig, Nat. Mater. **11**, 284 (2012).
[10] W. Wu, Y. Horibe, N. Lee, S.-W. Cheong, and J. R. Guest, Phys. Rev. Lett. **108**, 077203 (2012).
[11] O. D. Lavrentovich, Liq. Cryst. **24**, 117 (1998).
[12] M. Fiebig, T. Lottermoser, D. Fröhlich, A. V. Goltsev, and R. V. Pisarev, Nature (London) **419**, 818 (2002).
[13] F.-T. Huang, X. Y. Wang, S. M. Griffin, Y. Kumagai, O. Gindele, M.-W. Chu, Y. Horibe, N. A. Spaldin, and S.-W. Cheong, Phys. Rev. Lett. **113**, 267602 (2014).
[14] S. Brazovski and N. Kirova, J. Phys. IV (France) **9**, 10 (1999).
[15] I. E. Dzyaloshkinskii, JETP Lett. **25**, 2 (1977).
[16] T. Choi, Y. Horibe, H. T. Yi, Y. J. Choi, W. Wu, and S.-W. Cheong, Nat. Mater. **9**, 253 (2010).
[17] B. B. Van Aken, T. T. M. Palstra, A. Filippetti, and N. A. Spaldin, Nat. Mater. **3**, 164 (2004).
[18] Y. Kumagai and N. A. Spaldin, Nat. Commun. **4**, 1540 (2013).
[19] S. M. Griffin, M. Lilienblum, K. T. DelaneyY. Kumagai, M. Fiebig, and N. A. Spaldin, Phys. Rev. X **2**, 041022 (2012).
[20] S.-Z. Lin *et al.*, Nat. Phys. **10**, 970 (2014).
[21] M. Lilienblum, T. Lottermoser, S. Manz, S. M. Selbach, A. Cano, and M. Fiebig, Nat. Phys. **11**, 1070 (2015).
[22] J. Li, F.-K. Chiang, Z. Chen, C. Ma, M.-W. Chu, C.-H. Chen, H. F. Tian, H. X. Yang, and J. Q. Li, Sci. Rep. **6**, 28047 (2016).
[23] M.-G. Han, Y. Zhu, L. Wu, T. Aoki, V. Volkov, X. Wang, S. C. Chae, Y. S. Oh, and S.-W. Cheong, Adv. Mater. **25**, 2415 (2013).
[24] J. Li, H. X. Yang, H. F. Tian, S. W. Cheong,, C. Ma, S. Zhang, Y. G. Zhao, and J. Q. Li, Phys. Rev. B **87**, 094106 (2013).
[25] S. C. Chae, Y. Horibe, D. Y. Jeong, S. Rodan, N. Lee, and S.-W. Cheong, Proc. Natl. Acad. Sci. U.S.A. **107**, 21366 (2010).
[26] F. Xue, X. Y. Wang, I. Socolenco, Y. J. Gu, L.-Q. Chen, and S.-W. Cheong, Sci. Rep. **5**, 17057 (2015).
[27] See Supplemental Material http://link.aps.org/supplemental/10.1103/PhysRevLett.118.145501 for detailed analyses about the vortex structures and simulations, which includes Refs. [28–34].
[28] Z. C. Wang, M. Saito, K. P. McKenna, and Y. Ikuhara, Nat. Commun. **5**, 3239 (2014).
[29] C. W. Zhao, Y. M. Xing, C. E. Zhou, and P. C. Bai, Acta Mater. **56**, 2570 (2008).
[30] Y. Y. Zhu, C. Ophusb, J. Cistonb, and H. Y. Wanga, Acta Mater. **61**, 5646 (2013).
[31] G. Bárcena-González, M. P. Guerrero-Lebrero, E. Guerrero, D. Fernández-Reyes, D. González, A. Mayoral, A. D. Utrilla, J. M. Ulloa, and P. L. Galindo, J. Microsc. **262**, 50 (2016).

[32] M. Arredondo, Q. M. Ramasse, M. Weyland, R. Mahjoub, I. Vrejoiu, D. Hesse, N. D. Browning, M. Alexe, P. Munroe, and V. Nagarajan, Adv. Mater. **22**, 2430 (2010).
[33] J. Li, C. Zhao, Y. Xing, S. Su, and B. Cheng, Materials **6**, 2130 (2013).
[34] A. M. Sanchez, P. L. Galindo, S. Kret, M. Falke, R. Beanland, and P. J. Goodhew, J. Microsc. **221**, 1 (2006).
[35] M. J. Hÿtch, E. Snoeck, and R. Kilaas, Ultramicroscopy **74**, 131 (1998).
[36] S. Cheng, Y. G. Zhao, X. F. Sun, and J. Zhu, J. Am. Ceram. Soc. **97**, 3371 (2014).
[37] C. J. Fennie and K. M. Rabe, Phys. Rev. B **72**, 100103(R) (2005).
[38] S. Artyukhin, K. T. Delaney, N. A. Spaldin, and M. Mostovoy, Nat. Mater. **13**, 42 (2013).
[39] R. Peierls, Proc. Phys. Soc. London **52**, 34 (1940).
[40] F. R. N. Nabarro, Proc. Phys. Soc. London **59**, 256 (1947).
[41] Z. S. Dong and C. W. Zhao, Physica (Amsterdam) **405B**, 171 (2010).
[42] R. Kutka and H.-R. Trebin, J. Phys. (Paris), Lett. **45**, 1119 (1984).
[43] R. Kutka, H.-R. Trebin, and M. Kiemes, J. Phys. (Paris) **50**, 861 (1989).
[44] H. R. Trebin, Adv. Phys. **31**, 195 (1982).
[45] V. P. Mineev, *Topologically Stable Defects and Solitons in Ordered Media* (Harwood Academic, Chur, Switzerland, 1998).